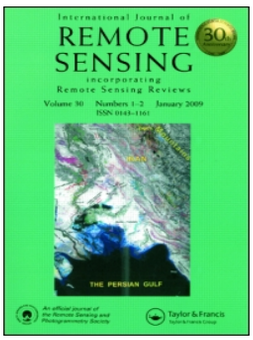

International Journal of Remote Sensing

ISSN: 0143-1161 (Print) 1366-5901 (Online) Journal homepage: http://www.tandfonline.com/loi/tres20

Improvement of land-cover classification over frequently cloud-covered areas using Landsat 8 time-series composites and an ensemble of supervised classifiers

Chuc Duc Man, Thuy Thanh Nguyen, Hung Quang Bui, Kristofer Lasko & Thanh Nhat Thi Nguyen

To cite this article: Chuc Duc Man, Thuy Thanh Nguyen, Hung Quang Bui, Kristofer Lasko & Thanh Nhat Thi Nguyen (2018) Improvement of land-cover classification over frequently cloud-covered areas using Landsat 8 time-series composites and an ensemble of supervised classifiers, International Journal of Remote Sensing, 39:4, 1243-1255

To link to this article: https://doi.org/10.1080/01431161.2017.1399477

Published online: 20 Nov 2017.

INTERNATIONAL JOURNAL OF REMOTE SENSING, 2017
VOL. 39, NO. 4, 1243–1255
https://doi.org/10.1080/01431161.2017.1399477

Taylor & Francis
Taylor & Francis Group

Improvement of land-cover classification over frequently cloud-covered areas using Landsat 8 time-series composites and an ensemble of supervised classifiers

Chuc Duc Man[a], Thuy Thanh Nguyen[a], Hung Quang Bui[a], Kristofer Lasko[b] and Thanh Nhat Thi Nguyen[a]

[a]Center of Multidisciplinary Integrated Technologies for Field Monitoring, University of Engineering and Technology – Vietnam National University, Hanoi, Vietnam; [b]Department of Geographical Sciences, University of Maryland, College Park, United States of America

ABSTRACT

Recent abundance of moderate-to-high spatial resolution satellite imagery has facilitated land-cover map production. However, in cloud-prone areas, building high-resolution land-cover maps is still challenging due to infrequent satellite revisits and lack of cloud-free data. We propose a classification method for cloud-persistent areas with high temporal dynamics of land-cover types. First, compositing techniques are employed to create dense time-series composite images from all available Landsat 8 images. Then, spectral–temporal features are extracted to train an ensemble of five supervised classifiers. The resulting composite images are clear with at least 99.78% cloud-free pixels and are 20.47% better than their original images on average. We classify seven land classes, including paddy rice, cropland, grass/shrub, trees, bare land, impervious area, and waterbody over Hanoi, Vietnam, in 2016. Using a time series of composites significantly improves the classification performance with 10.03% higher overall accuracy (OA) compared to single composite classifications. Additionally, using time series of composites and the ensemble technique, which combines the best of five experimented classifiers (eXtreme Gradient Boosting, logistic regression, Support Vector Machine (SVM) with Radial Basis Function (RBF) kernel – SVM–RBF and Linear kernel – SVM–Linear, multilayer perceptron), performed best with 84% OA and 0.79 kappa coefficient.

ARTICLE HISTORY
Received 30 May 2017
Accepted 17 October 2017

1. Introduction

Land-cover classification (LCC) mapping is now easier due to availability of multi-satellite imagery such as Landsat 5/7/8 (Wulder et al. 2012). However, in cloud-prone areas, deriving high-resolution LCC maps from optical imagery is challenging because of infrequent satellite revisits and lack of cloud-free data. This is even more pronounced in land cover with high temporal dynamics, that is, paddy rice or seasonal crops, which require observation of key growing stages to correctly identify (Le Toan et al. 1997;

CONTACT Chuc Duc Man chucmd@fimo.edu.vn

Kontgis, Schneider, and Ozdogan 2015). Recently, a number of best-available-pixel compositing (BAP) methods have been proposed to eliminate effects of cloud in LCC using medium or high resolution satellite images. Generally, BAP methods replace cloudy pixels with best-quality pixels from a set of candidates through rule-based procedures. Selection rules are based on spectral-related information, that is, maximum normalized difference vegetation index (NDVI) (Roy et al. 2010) and median near-infrared (NIR) (Potapov, Turubanova, and Hansen 2011). On another approach, Griffiths et al. (2013) proposed a BAP method ranking candidate pixels by score set such as distance to cloud/cloud shadow, year, and day-of-year (DOY). This method was improved by incorporating new scores for atmospheric opacity and sensor types (White et al. 2014). Gómez, White, and Wulder (2016) recently offered a review emphasizing BAP potential for monitoring in cloud-persistent areas, which includes applications in forest biomass, recovery and species mapping (Pickell et al. 2015; Thompson et al. 2015; Zald et al. 2016), change detection applications (Hermosilla et al. 2015), and general land-cover applications (Franklin et al. 2015).

Vietnam is located in a tropical monsoon climate frequently covered by cloud (Whitcraft et al. 2015; Nguyen, Bui, et al. 2015). Previous studies employed single-image classifications (Ngo, Mai, and Pedrycz 2015). However, common challenges of mono-temporal approaches include misclassification between bare land or impervious surface and vegetation cover type (Henits, Jürgens, and Mucsi 2016), whereas LCC using cloud-free Landsat scenes may lack enough observations to capture temporal dynamics of land-cover types.

We propose a classification method for cloud-prone areas with high temporal dynamics of land-cover types. First, we construct dense time-series BAP composites using all available Landsat 8 images. Next, spectral–temporal features are extracted from the composited images to train advanced supervised classifiers including eXtreme Gradient Boosting (XGBoost), logistic regression (LR), Support Vector Machine (SVM) with RBF kernel (SVM–RBF) and Linear kernel (SVM–Linear), and multilayer perceptron (MLP). The best-performing models are selected to create an ensemble model to further improve classification performance.

2. Methodology

2.1. *Study area*

Hanoi is the capital of Vietnam, the country's second largest city covering approximately 3300 km^2, located in the centre of Red River Delta (RRD). Hanoi has three basic kinds of terrain including a fertile delta, midland region, and mountainous zone. Hanoi is mainly divided into agricultural area (56.6%) and non-agricultural area (40.6%) in 2010 (Government of Vietnam 2013). In agricultural areas, paddy rice is dominant (60.9%) followed by other crops such as maize as well as various vegetable crops. Paddy rice is planted two times per year, while crops are grown in other dedicated areas. Occasionally, short-season vegetable crops or aquaculture are grown before the start of the first rice season. Non-agricultural areas are mostly covered by impervious surfaces and mosaicked natural landscape. Accordingly, we investigate seven LC classes for Hanoi including paddy rice, cropland, grass/shrub, trees, bare land, impervious area, and waterbody.

2.2. *Reference data*

We use official land-use data from Hanoi Environment and Natural Resources Department for training and testing data selection (Hanoi Environment and Natural Resources Department 2014). Since different land uses may contain the same land-cover types, we generated 11 strata labelled as bare area, long-term crops, short-term crops, forest, grass, impervious area, mudflats, rice, water, others, and overlap areas of the land-use strata. Training and testing data are randomly sampled from the strata and then labelled into seven classes using high-resolution images of Google Earth and field data. Total numbers of training and testing data are 5079 and 2748 points with the following training and testing point distribution: crop (596, 331), bare land (75, 56), paddy rice (1195, 646), waterbody (773, 446), tree (997, 491), impervious area (1049, 523), and grass/shrub (394, 255).

2.3. *Landsat 8 surface reflectance (L8SR) compositing*

To prepare imagery for the 2016 Hanoi land-cover map, all L8SR images from 2013 to 2016 are collected from USGS Earth Explorer (https://earthexplorer.usgs.gov/). There are 54 available L8SR scenes which are not 100% cloud-contaminated. As Hanoi is covered by two consecutive L8SR scenes per revisit, the resulting 27 images are mosaicked (Figure 1). The purpose of this step is to generate a dense, cloud-free time series to capture major spectral variations for 2016 LCC. The target images for compositing were the five clearest L8SR images from: 16 May 2016 (DOY 137), 1 June 2016 (DOY 153), 17 June 2016 (DOY 169), 21 September 2016 (DOY 265), and 7 October 2016 (DOY 281). These images were the targets for the compositing process which replaces their own

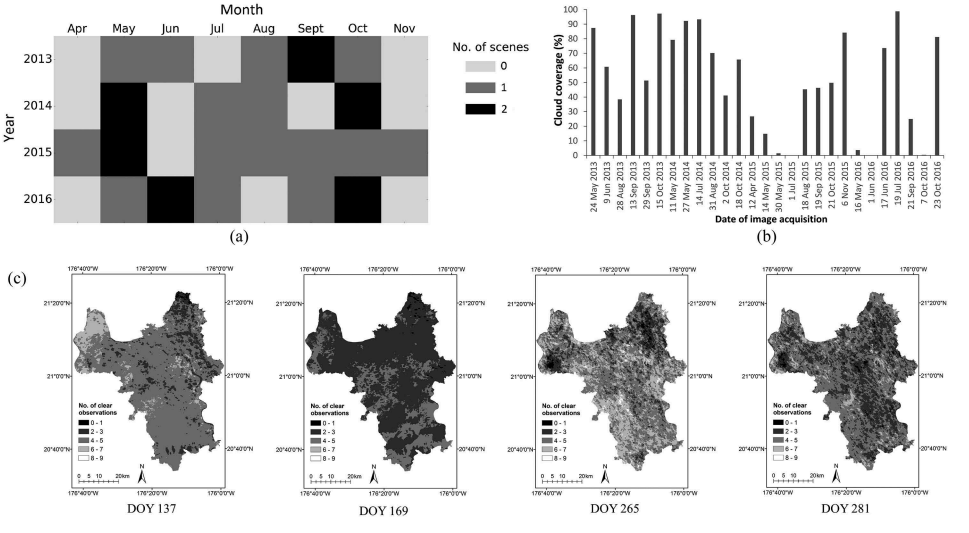

Figure 1. (a) Distribution of L8SR images from 2013–2016 over Hanoi, (b) cloud cover statistics per L8SR image, and (c) clear observation count maps for each image used in the compositing process (DOY 137, 169, 265, 281).

cloud/cloud shadow pixels with best-quality pixels from the above potential candidate images based on a scoring method described below.

For each target image, clear pixels remain while cloudy pixels are replaced by a clear observation selected from the candidates. We combine two BAP methods proposed in Griffiths et al. (2013) and White et al. (2014) and modify the opacity score for compatibility with L8SR data. For each clear pixel in a candidate image, a score is computed based on four sub-scores: year score, DOY score, opacity score, and distance from cloud/cloud shadow pixel. Year score, DOY score, and distance to cloud/cloud shadow are computed following Griffiths et al. (2013). Year scores decrease with distance from target year (2016) to support years (2015, 2014, 2013). DOY scores reflect ranges of target day and support days following Gaussian distribution. Distance to cloud/cloud shadow is calculated by a Sigmoid function of distances from the pixel to cloud/cloud shadow, obtained from the file sr_cfmask (Zhu, Wang, and Woodcock 2015), in radius of 50 pixels around. The opacity score requires an aerosol image as input (White et al. 2014), but L8SR provides only discrete aerosol information (i.e. four aerosol levels) in the sr_cloud files. Therefore, we assign opacity scores to the aerosol levels using a Sigmoid function. Finally, a pixel's score is derived by summing the four sub-scores. The candidate pixel owning the greatest score is chosen to replace the clouded pixel in the target image (Table 1).

2.4. *Land-cover classification*

Three classification methods are investigated as in Figure 2. First, an XGBoost classifier is applied on seven spectral bands of each composite image to obtain five LC maps for 2016. The second is time-series classification using XGBoost classifier on stack of seven spectral bands of five composites (i.e. 35 spectral–temporal features). After that, they are compared to assess if a time series of composites is better than individual composites for classification. The third improves the time-series composite classification by adding mean standard deviations (MSDs) of each band calculated from the composites. Five single classifiers (XGBoost, LR, SVM–RBF, SVM–Linear, and MLP) and an ensemble model using majority voting (i.e. predicted class labels are voted by five classifiers having the same weight) are compared. The selection of these classifiers is due to wide applications for LCC using SVM and MLP (Foody and Mathur 2004; Kavzoglu and Mather 2003) and LR (Mallinis and Koutsias 2008) reported in literature. Additionally, XGBoost is investigated due to novelty (Chen and Guestrin 2016) and current lack of LCC applications.

All of these classifiers have specific hyper-parameters that require tuning for the best classification performance. Specifically, SVM–RBF's hyper-parameters are penalty (*C*) and

Table 1. Summary of year score, DOY score, opacity score and distance to cloud/cloud shadow for L8SR composition.

Year			Opacity		
Score	Description	DOY	Score	Description	Distance to cloud/cloud shadow
1.00	2016	Constraint is ± 30 days from target day. Scoring by a Gaussian function.	0.023	High aerosol content	Constraint is 50 pixel radius from considered pixel. Scoring by a Sigmoid function.
0.68	2015		0.223	Average aerosol content	
0.42	2014		0.777	Low aerosol content	
0.22	2013		0.977	Climatology-level aerosol content	

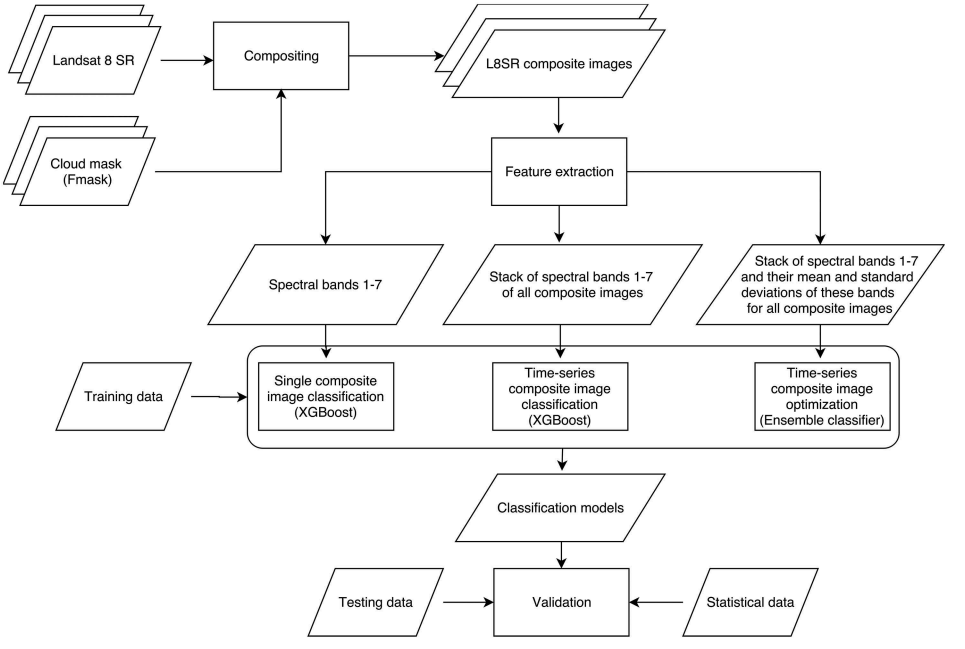

Figure 2. Overall flow chart of the study methodology.

gamma. SVM–Linear requires penalty (*C*) only. Important hyper-parameters forming a base architecture of MLP include activation function (activation), number of hidden layers (hidden layers), and number of hidden nodes in individual hidden layers (hidden nodes). Similar to SVM, LR also has a regularization parameter (*C*) for individual training data importance (Hackeling 2017). XGBoost has many hyper-parameters in which the three most important ones are the number of boosted trees (n_estimators) and two others for over-fitting prevention: maximum tree depth (max_depth) and minimum sum of weights of all observations required in a child (min_child_weight).

All classifications were performed on the same training and testing points with 10-fold cross validation to select best hyper-parameters for each classifier. Then all training data are used to train classifiers with best parameters. Testing sets are separated from training sets to assess trained classifiers. We used scikit-learn implementation of the classifiers in our experiments (http://scikit-learn.org). Scikit-learn is a python-based machine learning library with robust tools and easy-to-use interface. Overall accuracy (OA), kappa coefficient, and F1 score (F1) are used as evaluation metrics in this study (Congalton and Green 2008; Powers 2011). Additionally, classification maps are validated against statistical data and visually examined.

3. Experiments and analysis

3.1. *Completeness of the composition*

Before composition, the average cloud percentage over five target images is 20.54% where image at DOY 169 is cloudiest with 73.63% cloud pixels. After compositing, all

images are at least 99.78% clear (i.e. DOY 265). However, there are remaining cloudy pixels without replacement candidates. The data of 2015 mostly contribute to composition with 72.36%, followed by 2013 (22.04%), 2014 (5.55%), and 2016 (0.05%) data.

Although pixel candidates are carefully selected by BAP, they are still spectrally different from neighbouring pixels of other candidate images. For example, for DOY 265 in Figure 4(b), composite pixels over a rice planting area show different colour blocks. Some cloudy pixels are replaced by vegetated observations, while others are replaced by flooded observations. This indicates selection of appropriate images has significant impact on BAP composites for areas with a high temporal dynamic of land-cover types, especially rice and agricultural areas. Thus, knowledge of local agricultural calendar could improve image selection for spectrally uniform BAP composites.

3.2. *Phenological analysis of land-cover classes*

NDVI and Bare Soil Index (BSI) temporal profiles of seven land-cover classes are presented in Figure 3. Seven classes can be divided into four distinct groups: impervious area, bare land; paddy rice; water; and tree, crop, grass, and shrub. Due to cultivation practices, paddy rice's NDVI and BSI temporal profile varies across the year. The remaining trends are shown in Figure 3.

3.3. *Classification accuracy*

3.3.1. *Yearly single composite classification versus yearly time-series composite classification*

Test set validation results are provided in Table 2. We found classifications using time-series composites outperformed all single-image classifications with 10.03% higher OA and 0.13 higher kappa coefficient on average. Single-image classification is also unstable as the results range 68.43–76.38% for OA and 0.59–0.68 for kappa coefficient. We found three out five single-image classifications achieved greater than 72% OA, except for the DOY169 and DOY265 which have large BAP pixels included with 73.60% and 24.76%, respectively.

Considering per-class accuracy, classification of vegetation classes is significantly improved with time-series classification, as those classes have high temporal dynamics best captured by multiple observations (Arvor et al. 2011; Kontgis, Schneider, and Ozdogan 2015). From the results, rice in green stage in DOYs of 137, 153, and 265 is most confused with crop and grass/shrub (see Figure 4(c)). In DOY 169, rice fields are flooded, thus resulting in confusion of rice and water. In the last image, DOY 281, harvested rice is confused with bare land and impervious area (Figure 4(c)). By integrating all confusing information in time-series classification, rice are better separated from other vegetation classes with F1 = 0.91 (Figure 4(d)).

Although most LC classes are better identified in time-series classification, bare land had confusion with impervious area (maximum F1 = 0.26, the time series F1 = 0.22). This is attributed to the two classes having spectrally similar and stable reflectance through time, and a low number of training samples for bare land. Crop and grass/shrub are occasionally misclassified due to similar spectral signals and mixed pixels. Water is separable from other classes due to its unique spectral properties, but some waterbodies

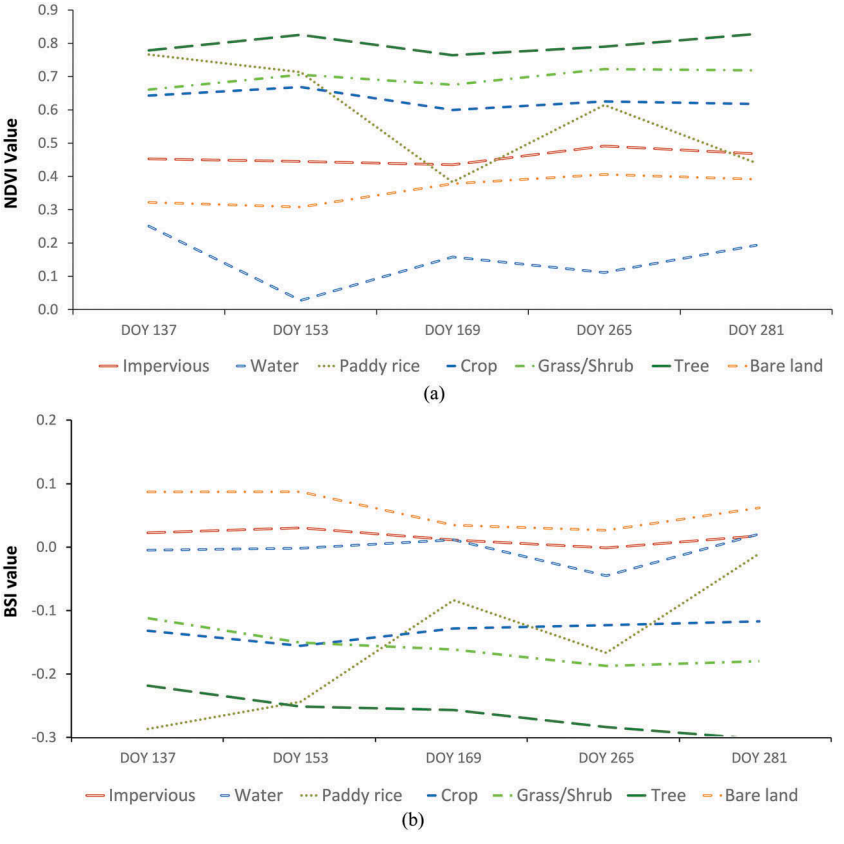

Figure 3. Land cover based: (a) NDVI temporal profiles and (b) BSI temporal profiles.

Table 2. F1 score, F1 score average, OA, and kappa coefficient for seven land-cover classes of six classification cases obtained using XGBoost.

	DOY 137	DOY 153	DOY 169	DOY 265	DOY 281	Time series
Crop	0.50	0.39	0.36	0.33	0.40	**0.58**
Bare land	0.06	**0.26**	0.04	0.17	0.14	0.22
Paddy rice	0.87	0.84	0.81	0.73	0.80	**0.91**
Water	0.85	0.86	0.73	0.81	0.83	**0.91**
Tree	0.67	0.70	0.66	0.65	0.74	**0.80**
Impervious area	0.84	0.87	0.78	0.83	0.86	**0.90**
Grass/Shrub	0.36	0.29	0.30	0.27	0.28	**0.44**
F1 score average	0.76	0.74	0.69	0.68	0.73	**0.82**
OA (%)	76.4	75.7	69.7	68.4	73.6	**82.8**
kappa coefficient	0.68	0.68	0.61	0.59	0.66	**0.77**

Best classification cases are written in bold.

are seasonally vegetated, leading to misclassification of water and vegetation. Thus, water also benefits from multiple image observations.

3.3.2. *Improvement of ensemble model against single-classifier model*

For ensemble classification, the following single models with their optimized parameters are employed: (i) XGBoost with n_estimators = 1000, max_depth = 5,

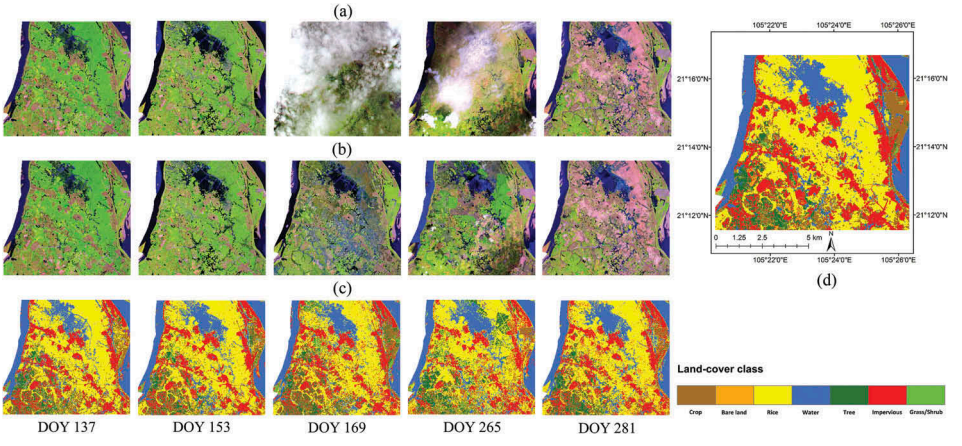

Figure 4. (a) Original surface reflectance images, (b) composite images, (c) classification maps for each image, and (d) classified map obtained from time-series composite images.

min_child_weight = 1; (ii) LR with C = 1; (iii) SVM–RBF with C = 10, gamma = 0.03125; (iv) SVM–Linear with C = 8; and (v) MLP with activation = tank, hidden layers = 1, and hidden nodes = 40. Classifiers perform on a stack of 35 spectral–temporal features and 7 MSDs of spectral bands. Majority voting technique is employed for the ensemble model.

Using an ensemble of supervised classifiers improves the classification (Table 3). We found individual models have similar accuracies with SVM–Linear lowest at 81.94% OA and XGBoost highest with 83.23% OA. The ensemble model is better than all individual models with OA = 83.96% and kappa coefficient = 0.79. Per-class accuracies of the ensemble model filter the best results from all single-classifier models. Classifier F1 score performance is presented in Figure 5. XGBoost is not effective at classifying bare land (F1 = 0.23) and grass/shrub (F1 = 0.4), but this disadvantage is overcome by SVM–RBF and SVM–Linear with F1 of 0.35, 0.46 for bare land, and 0.47, 0.49 for grass/shrub respectively. SVM–RBF and SVM–Linear are generally high performing. Paddy rice, impervious area, water, and tree have similar accuracies between classifiers which could be explained as the classes are quite separable in this time-series domain. MLP is overall good compared to other classifiers, but it performs poorly on bare land (F1 = 0.27). Ensemble model achieved similar accuracies of paddy rice, water, tree, and impervious areas as compared to other classifiers. However, for crop, grass/shrub, and bare land which are easily confused with other classes (Figure 3), ensemble model generally achieved better classification accuracies than any single-classifier model. By integrating models, individual strengths remain, while weaknesses are reduced. Table 4

Table 3. OA, kappa coefficient, F1 score average for each single-classifier and ensemble model.

	Classifier					
Measure	XGBoost	LR	SVM–RBF	SVM–Linear	MLP	Ensemble
OA (%)	83.2	82.6	82.9	81.9	83.1	**84.0**
kappa coefficient	0.77	0.77	0.78	0.77	0.78	**0.79**
F1 score average	0.82	0.82	0.83	0.83	0.83	**0.84**

Best classification cases are written in bold.

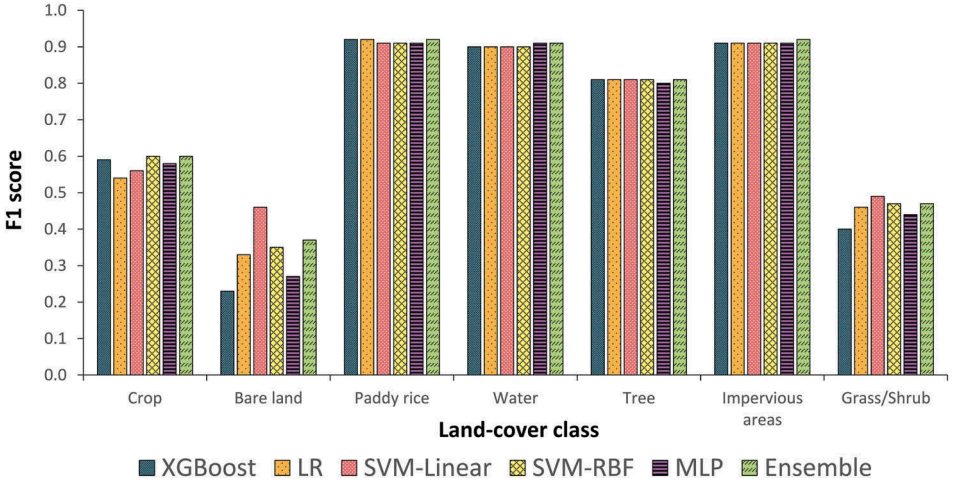

Figure 5. F1 score for land-cover class obtained using multiple classifiers.

presents confusion matrix of the ensemble model with user accuracy (UA) and producer accuracy (PA) for each class.

3.4. *Map validation*

The LC map of the ensemble model is displayed in Figure 6. We found that paddy rice and impervious area are the dominant classes. According to Office (2016), rice area in Hanoi for the spring-summer season is approximately 99,454 ha. We computed rice area for the classification maps and compared to the official statistic. The ensemble rice map is closest to the official number and slightly overestimates by 4764 ha (4.79%). Additional classifiers are shown in Table 5.

4. Discussion and conclusion

We developed a classification procedure for cloud-prone areas with a high temporal dynamic of land-cover types. The dense time-series composite images are constructed from all available multi-year Landsat 8 images over Hanoi. Then, we built an ensemble of five supervised classifiers to classify land-cover area into seven classes. Our best

Table 4. Confusion matrix of ensemble model.

	Crop	Bare land	Rice	Water	Tree	Impervious	Grass/Shrub	Reference total	UA (%)
Crop	**222**	3	25	4	24	22	31	331	66.1
Bare land	6	**22**	1	1	0	22	4	56	33.5
Rice	37	0	**581**	16	2	3	7	646	91.6
Water	5	0	11	**411**	4	11	4	446	90.9
Tree	26	2	3	2	**433**	8	17	491	83.2
Impervious	19	6	4	3	5	**485**	1	523	93.1
Grass/Shrub	56	7	12	5	47	11	**117**	255	38.9
Classification total	371	40	637	442	515	562	181	**2748**	**OA (%)**
PA (%)	55.1	41.0	92.8	92.0	79.3	90.5	59.8	**OA (%)**	**84.0**

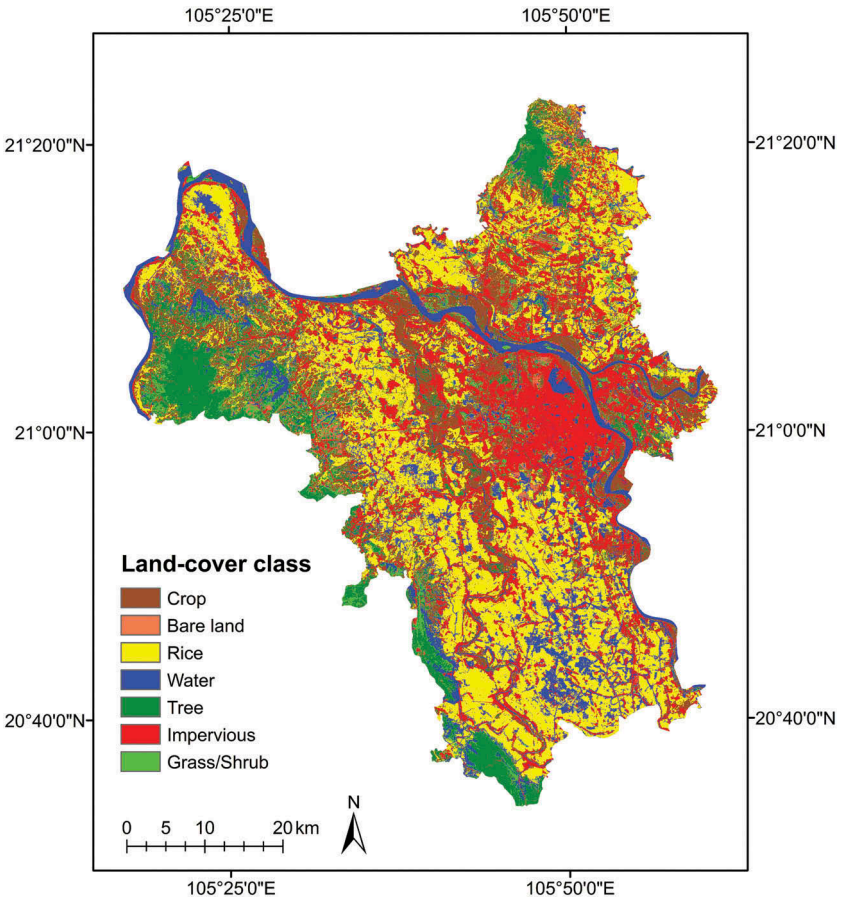

Figure 6. 2016 Land-cover map for Hanoi based on the most accurate classification using time-series composite imagery and the ensemble of five classifiers.

Table 5. Error (ha and %) of rice-mapped area for different classification scenarios.

Classification	DOY 137 composite	DOY 153 composite	DOY 169 composite	DOY 265 composite	DOY 281 composite	Time series of composites	Time series of composites with optimization
Error(ha)	+8657	+13,510	+15,674	+16,785	+8990	+7811	+4764
Error(%)	8.70	13.58	15.76	16.88	9.04	7.85	4.79

land-cover map using the ensemble model achieved 83.91% OA with kappa coefficient of 0.79. This is in comparison to 72% OA using the unmodified compositing algorithm in a slightly larger region and a few additional land-cover types (Griffiths et al. 2013). Additional regional land-cover mapping studies had generally good accuracy with: 89% OA for forest/non-forest cover maps (Potapov, Turubanova, and Hansen 2011), 90% OA for urban landscape with dense time-series stack (Castrence et al. 2014), 89% OA for land-cover map in a less-cloudy region with automated preprocessing and random forest (Mack et al. 2017), 89.42% OA in a recent rice/non-rice cover study over RRD with dense Landsat 8 time-series stack (Man et al. 2017), and

84% OA in a recent land-cover study over Hanoi employing radar to overcome clouds (Nguyen, Wagner, et al. 2015).

In summary, multi-year composition increases cloud-free pixels in composites, especially over cloud-persistent areas such as Hanoi, Vietnam. We developed time-series composites with over 99% cloud-free pixels. One disadvantage of this compositing is that it does not account for intra-annual vegetation phenology. However, using time-series composites still improves classification performance in comparison with any single composite classification. This is attributed to the effective representation of seasonal temporal dynamics of land-cover types. Among the top supervised classifers, XGBoost performed best for land-cover mapping. However, an ensemble model still improved classification results by promoting individual strengths and reducing weaknesses. In the future, image composition accounting for phenology could improve composite quality and classification accuracy for improved mapping of land-cover types with high temporal dynamics.

Acknowledgements

This work has been supported by Vietnam National University, Hanoi (VNU) (Project No. QG.17.41).

Disclosure statement

No potential conflict of interest was reported by the authors.

Funding

This work was supported by the Vietnam National University, Hanoi [No. QG.17.41];

References

Arvor, D., M. Jonathan, M. S. Penello, V. Dubreuil, and L. Durieux. 2011. "Classification of MODIS EVI Time Series for Crop Mapping in the State of Mato." *International Journal of Remote Sensing, No. December* 2014: 7847–7871. doi:10.1080/01431161.2010.531783.

Castrence, M., D. Nong, C. Tran, L. Young, and J. Fox. 2014. "Mapping Urban Transitions Using Multi-Temporal Landsat and DMSP-OLS Night-Time Lights Imagery of the Red River Delta in Vietnam." *Land* 3 (1): 148–166. doi:10.3390/land3010148.

Chen, T., and C. Guestrin. March, 2016. "XGBoost: A Scalable Tree Boosting System". *arXiv*. doi:10.1145/2939672.2939785. https://arxiv.org/abs/1603.02754

Chuc, M. D., N. H. Anh, N. T. Thuy, B. Q. Hung, and N. T. N. Thanh. 2017. "Paddy Rice Mapping in Red River Delta Region Using Landsat 8 Images: Preliminary Results." *The 9th International Conference on Knowledge and Systems Engineering (KSE2017)*. Hue, Vietnam: IEEE.

Congalton, R. G., and K. Green. 2008. *Assessing the Accuracy of Remotely Sensed Data: Principles and Practices*. Boca Raton: CRC Press, Taylor & Francis Group.

Foody, G. M., and A. Mathur. 2004. "A Relative Evaluation of Multiclass Image Classification by Support Vector Machines." *IEEE Transactions on Geoscience and Remote Sensing* 42 (6): 1335–1343. doi:10.1109/TGRS.2004.827257.

Franklin, S. E., O. S. Ahmed, M. A. Wulder, J. C. White, T. Hermosilla, and N. C. Coops. 2015. "Large Area Mapping of Annual Land Cover Dynamics Using Multitemporal Change Detection and

Classification of Landsat Time Series Data." *Canadian Journal of Remote Sensing* 41 (4): 293–314. doi:10.1080/07038992.2015.1089401.

Gómez, C., J. C. White, and M. A. Wulder. 2016. "Optical Remotely Sensed Time Series Data for Land Cover Classification: A Review." *ISPRS Journal of Photogrammetry and Remote Sensing* 116: 55–72. doi:10.1016/j.isprsjprs.2016.03.008.

Government of Vietnam. 2013. *Resolution on Landuse Planning from 2011-2015 and by 2020 for Hanoi*.

Griffiths, P., S. Van Der Linden, T. Kuemmerle, and P. Hostert. 2013. "A Pixel-Based Landsat Compositing Algorithm for Large Area Land Cover Mapping." *IEEE Journal of Selected Topics in Applied Earth Observations and Remote Sensing* 6 (5): 2088–2101. doi:10.1109/JSTARS.2012.2228167.

Hackeling, G. 2017. *Mastering Machine Learning with Scikit-Learn*. Birmingham, UK: Packt Publishing. https://www.packtpub.com/big-data-and-business-intelligence/mastering-machine-learning-scikit-learn-second-edition.

Hanoi Environment and Natural Resources Department. 2014. "Land Use Statistics of Hanoi." Accessed 20 December 2016. http://qhkhsdd.hanoi.gov.vn.

Hanoi Statistics Office. 2016. "Report of Socio-Economic Survey." Accessed 19 April 2017. http://thongkehanoi.gov.vn/.

Henits, L., C. Jürgens, and L. Mucsi. January, 2016. "Seasonal Multitemporal Land-Cover Classification and Change Detection Analysis of Bochum, Germany, Using Multitemporal Landsat TM Data." *International Journal of Remote Sensing* 1–16. Taylor & Francis. doi:10.1080/01431161.2015.1125558.

Hermosilla, T., M. A. Wulder, J. C. White, N. C. Coops, and G. W. Hobart. 2015. "An Integrated Landsat Time Series Protocol for Change Detection and Generation of Annual Gap-Free Surface Reflectance Composites." *Remote Sensing of Environment* 158 (March): 220–234. doi:10.1016/j.rse.2014.11.005.

Kavzoglu, T., and P. M. Mather. 2003. "The Use of Backpropagating Artificial Neural Networks in Land Cover Classification." *International Journal of Remote Sensing, No. December* 2014: 37–41. doi:10.1080/0143116031000114851.

Kontgis, C., A. Schneider, and M. Ozdogan. 2015. "Mapping Rice Paddy Extent and Intensification in the Vietnamese Mekong River Delta with Dense Time Stacks of Landsat Data." *Remote Sensing of Environment* 169: 255–269. Elsevier Inc. doi:10.1016/j.rse.2015.08.004.

Le Toan, T., F. Ribbes, L.-F. Wang, N. Floury, K.-H. Ding, J. A. Kong, M. Fujita, and T. Kurosu. 1997. "Rice Crop Mapping and Monitoring Using ERS-1 Data Based on Experiment and Modeling Results." *IEEE Transactions on Geoscience and Remote Sensing* 35 (1): 41–56. doi:10.1109/36.551933.

Mack, B., P. Leinenkugel, C. Kuenzer, and S. Dech. 2017. "A Semi-Automated Approach for the Generation of A New Land Use and Land Cover Product for Germany Based on Landsat Time-Series and Lucas *in-Situ* Data." *Remote Sensing Letters* 8(3): 244–253. Taylor & Francis. doi:10.1080/2150704X.2016.1249299.

Mallinis, G., and N. Koutsias. 2008. "Spectral and Spatial-Based Classification for Broad-Scale Land Cover Mapping Based on Logistic Regression." *Sensors* 8: 8067–8085. doi:10.3390/s8128067.

Ngo, L. T., D. S. Mai, and W. Pedrycz. 2015. "Semi-Supervising Interval Type-2 Fuzzy C-Means Clustering with Spatial Information for Multi-Spectral Satellite Image Classification and Change Detection." *Computers & Geosciences* 83: 1–16. Elsevier. doi:10.1016/j.cageo.2015.06.011.

Nguyen, D., W. Wagner, V. Naeimi, and S. Cao. 2015. "Rice-Planted Area Extraction by Time Series Analysis of ENVISAT ASAR WS Data Using A Phenology-Based Classification Approach: A Case Study for Red River Delta, Vietnam." In *Proceedings of the International Archives Photogrammetry, Remote Sensing and Spatial Information Science,* 11–15 May 2015, Berlin, Germany. doi:10.5194/isprsarchives-XL-7-W3-77-2015.

Nguyen, T. T. N., H. Q. Bui, H. V. Pham, H. V. Luu, D. C. Man, H. N. Pham, H. T. Le, and T. T. Nguyen. 2015. "Particulate Matter Concentration Mapping from MODIS Satellite Data: A Vietnamese Case Study." *Environmental Research Letters* 10(9): 95016. IOP Publishing. doi:10.1088/1748-9326/10/9/095016.

Pickell, P. D., T. Hermosilla, R. J. Frazier, N. C. Coops, and M. A. Wulder. 2015. "Forest Recovery Trends Derived from Landsat Time Series for North American Boreal Forests." *International Journal of Remote Sensing* 37(1): 138–149. Taylor & Francis. doi:10.1080/2150704X.2015.1126375.

Potapov, P., S. Turubanova, and M. C. Hansen. 2011. "Remote Sensing of Environment Regional-Scale Boreal Forest Cover and Change Mapping Using Landsat Data Composites for European Russia." *Remote Sensing of Environment* 115(2): 548–561. Elsevier Inc. doi:10.1016/j.rse.2010.10.001.

Powers, D. M. W. 2011. "Evaluation: From Precision, Recall and F-Measure to Roc, Informedness, Markedness & Correlation." *Journal of Machine Learning Technologies* 2 (1): 37–63.

Roy, D. P., J. Junchang, K. Kline, P. L. Scaramuzza, V. Kovalskyy, M. Hansen, T. R. Loveland, E. Vermote, and C. Zhang. 2010. "Remote Sensing of Environment Web-Enabled Landsat Data (WELD): Landsat ETM + Composited Mosaics of the Conterminous United States." *Remote Sensing of Environment* 114(1): 35–49. Elsevier Inc. doi:10.1016/j.rse.2009.08.011.

Thompson, S. D., T. A. Nelson, J. C. White, and M. A. Wulder. 2015. "Mapping Dominant Tree Species over Large Forested Areas Using Landsat Best-Available-Pixel Image Composites." *Canadian Journal of Remote Sensing* 41 (3): 203–218. doi:10.1080/07038992.2015.1065708.

Whitcraft, A. K., E. F. Vermote, I. Becker-Reshef, and C. O. Justice. 2015. "Cloud Cover Throughout the Agricultural Growing Season: Impacts on Passive Optical Earth Observations." *Remote Sensing of Environment* 156: 438–447. Elsevier Inc. doi:10.1016/j.rse.2014.10.009.

White, J. C., M. A. Wulder, G. W. Hobart, J. E. Luther, T. Hermosilla, P. Griffiths, N. C. Coops, et al. 2014. "Pixel-Based Image Compositing for Large-Area Dense Time Series Applications and Science." *Canadian Journal of Remote Sensing* 40 (3): 192–212. doi:10.1080/07038992.2014.945827.

Wulder, M. A., J. G. Masek, W. B. Cohen, T. R. Loveland, and C. E. Woodcock. 2012. "Remote Sensing of Environment Opening the Archive : How Free Data Has Enabled the Science and Monitoring Promise of Landsat." *Remote Sensing of Environment* 1–9. Elsevier B.V. doi:10.1016/j.rse.2012.01.010.

Zald, H. S. J., M. A. Wulder, J. C. White, T. Hilker, T. Hermosilla, G. W. Hobart, and N. C. Coops. 2016. "Integrating Landsat Pixel Composites and Change Metrics with Lidar Plots to Predictively Map Forest Structure and Aboveground Biomass in Saskatchewan, Canada." *Remote Sensing of Environment* 176 (April): 188–201. doi:10.1016/j.rse.2016.01.015.

Zhu, Z., S. Wang, and C. E. Woodcock. 2015. "Improvement and Expansion of the Fmask Algorithm : Cloud, Cloud Shadow, and Snow Detection for Landsats 4 – 7, 8, and Sentinel 2 Images." *Remote Sensing of Environment* Elsevier Inc. doi:10.1016/j.rse.2014.12.014.